Low-cost inkjet-printed nanostructured biosensor based on CRISPR/Cas12a system for pathogen detection

Angela Gilda Carota [a], Andrea Bonini [a,b,1,*], Massimo Urban [c], Noemi Poma [b], Federico Maria Vivaldi [a], Arianna Tavanti [b], Marianna Rossetti [c], Giulio Rosati [c], Arben Merkoçi [c,d], Fabio Di Francesco [a,**]

[a] Department of Chemistry and Industrial Chemistry, University of Pisa, Via Giuseppe Moruzzi 13, 56124 Pisa, Italy
[b] Department of Biology, University of Pisa, Via San Zeno 37, 56127 Pisa, Italy
[c] Catalan Institute of Nanoscience and Nanotechnology (ICN2), CSIC and BIST, Campus UAB, Bellaterra, 08193 Barcelona, Spain
[d] Catalan Institution for Research and Advanced Studies (ICREA), Passeig de Lluís Companys, 23, Barcelona, 08010, Spain

ABSTRACT

The escalating global incidence of infectious diseases caused by pathogenic bacteria, especially in developing countries, emphasises the urgent need for rapid and portable pathogen detection devices. This study introduces a sensitive and specific electrochemical biosensing platform utilising cost-effective electrodes fabricated by inkjet-printing gold and silver nanoparticles on a plastic substrate. The biosensor exploits the CRISPR/Cas12a system for detecting a specific DNA sequence selected from the genome of the target pathogen. Upon detection, the trans-activity of Cas12a/gRNA is triggered, leading to the cleavage of rationally designed single-strand DNA reporters (linear and hairpin) labelled with methylene blue (ssDNA-MB) and bound to the electrode surface. In principle, this sensing mechanism can be adapted to any bacterium by choosing a proper guide RNA to target a specific sequence of its DNA. The biosensor's performance was assessed for two representative pathogens (a Gram-negative, *Escherichia coli*, and a Gram-positive, *Staphylococcus aureus*), and results obtained with inkjet-printed gold electrodes were compared with those obtained by commercial screen-printed gold electrodes. Our results show that the use of inkjet-printed nanostructured gold electrodes, which provide a large surface area, in combination with the use of hairpin reporters containing a poly-T loop can increase the sensitivity of the assay corresponding to a signal variation of 86%. DNA targets amplified from various clinically isolated bacteria, have been tested and demonstrate the potential of the proposed platform for point-of-need applications.

1. Introduction

Pathogenic bacterial infections pose a significant global health threat, ranking as the second leading cause of death worldwide in 2019 (Ikuta et al., 2022). Developing countries are particularly susceptible, mainly due to contaminated water sources acting as vectors for infectious diseases (Ugboko et al., 2020; WHO, 2008, 2019), as well as to food and soil contamination (Santamaría and Toranzos, 2003; Tauxe, 2002). In this context, a timely detection of infections is critical (Barenfanger et al., 1999). Regrettably, conventional techniques such as culture-dependent methods (Douterelo et al., 2014) and widely employed molecular approaches, including PCR-based techniques, or mass spectrometry techniques, as MALDI-TOF (Rychert, 2019), exhibit limitations in terms of response time, cost and need of trained users (Ferone et al., 2020; Rajapaksha et al., 2019; Yang and Rothman, 2004). In this scenario, biosensors may be a practical alternative for promptly addressing on-site pathogen infections (Bonini et al., 2022). Numerous Point-of-Care (PoC) biosensors devices have been developed according to the ASSURED criteria (Land et al., 2018). These devices integrate portable optical and electrochemical transducers with the specificity of diverse biological receptors, including enzymes, aptamers, and antibodies (Cesewski and Johnson, 2020; Yoo and Lee, 2016). A decade after
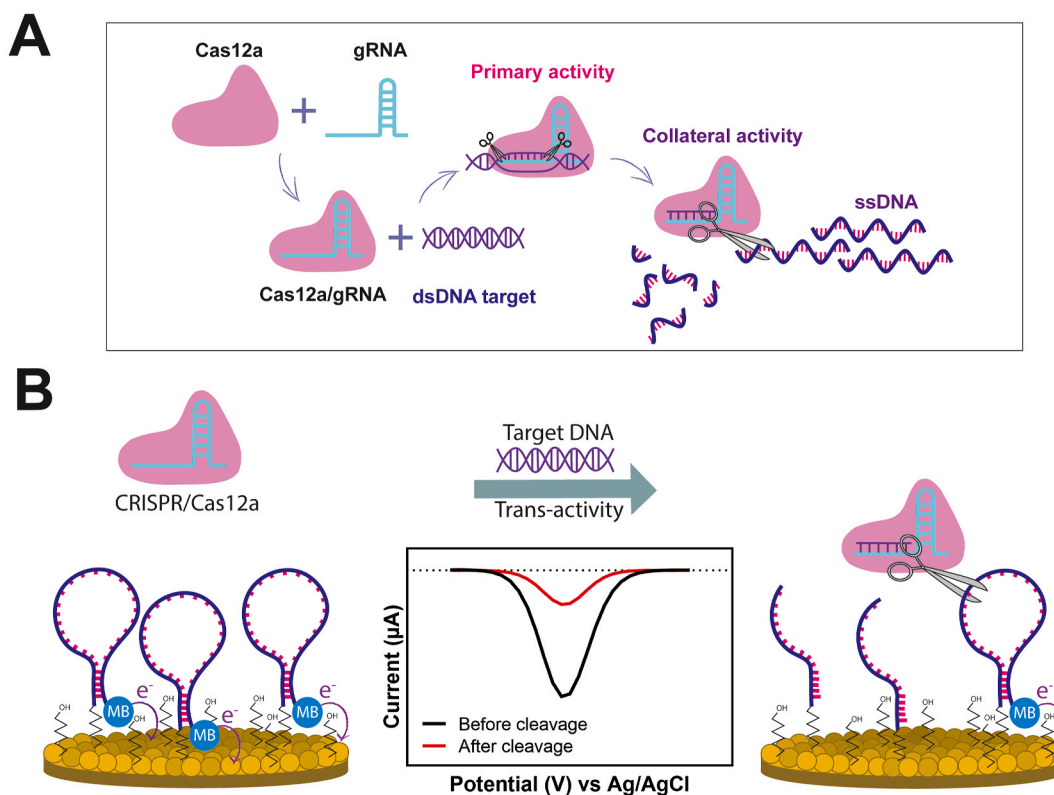
Fig. 1. Cas12a/gRNA Activation and Assay Detection Mechanism. *(A) Scheme illustrating the activation of both primary (i.e., cis-activity) and collateral activities (i.e., trans-activity) for the Cas12a/gRNA system. (B) Detection mechanism of the Inkjet-printed based CRISPR/Cas12a biosensor.*

Doudna and Charpentier introduced the CRISPR/Cas system for gene editing applications (Jinek et al., 2012), the number of relevant publications has exponentially increased across various fields (Tyumentseva et al., 2023). This growth is particularly evident in biosensor development, where the system's high specificity and programmability have been extensively applied (Bonini et al., 2021b; Cheng et al., 2022; Li et al., 2019). The CRISPR/Cas system operates as a nucleic acid-based adaptive immune system, providing defence for archaea and bacteria against bacteriophage infections, as it prevents the replication of the invader nucleic acid (Amitai and Sorek, 2016; Patterson et al., 2017; Rath et al., 2015). Within these microbial defence systems, different classes of endonuclease enzymes with varying mechanisms have been discovered. For example, Type II Cas9 exhibits only cis-activity, which involves the specific cleavage of the target nucleic acid. In contrast, enzymes belonging to Type V, such as Cas12a and Cas12 b, or to Type VI, in addition to the usual cis-activity, demonstrate a non-specific endonuclease collateral activity (trans-activity) triggered by the formation of the crRNA guide:target sequence complex (Chen et al., 2018; Swarts and Jinek, 2019) (Fig. 1A). Even though these enzymes share the same mechanism, some differences within and between the two classes can be observed. For instance, Cas12 b is a dual-RNA-guided endonuclease, while Cas12a is single-RNA-guided (Mao et al., 2022). Additionally, Type V enzymes are activated by and are selective for DNA, while Cas13 acts on RNA. All these differences have been utilized to develop specific biosensing techniques (Aman et al., 2020). Several detection strategies have been developed in recent years based on the combination of optical and electrochemical transducers and CRISPR/Cas systems for the detection of nucleic acids (Ma et al., 2023; Swetha et al., 2021; Zavvar et al., 2022). For example, optical biosensors using both fluorescence and colorimetric approaches have exploited the collateral activity of Cas12 or Cas13 for the detection of DNA and RNA, respectively (Granados-Riveron et al., 2021; Mukama et al., 2020). The detection mechanism typically involves oligonucleotide reporters labelled with a fluorophore and a quencher. Upon recognition of the target nucleic acid, the activation of the non-specific endonuclease activity produces a fluorescence signal as the reporters undergo cleavage, achieving atto-molar detection limit when coupled to isothermal amplification methods (Gootenberg et al., 2017). Typically, the incorporation of nanomaterials is employed to enhance the biosensor's performance. For instance, the aggregation or dispersion of suitably functionalized gold nanoparticles facilitates the colorimetric detection and aligns the outcomes with the qPCR results (Ki et al., 2022; Ma et al., 2023; Wang et al., 2022). Significant efforts have been directed towards electrochemical transduction for its facile implementation in low-cost and portable devices (Xu et al., 2020). Various strategies have been explored that involve the activation of Cas9 or Cas12 (Yudin Kharismasari et al., 2024) and the following interaction with a single-strand DNA (ssDNA) reporter labelled with a redox probe and bound to the surface of the working electrode. Notably, when the enzyme activation occurs, a discernible change in the current intensity at the redox peak of the label is observed (Dai et al., 2019). Alternatively, label-free methods detect changes in the charge transfer resistance (R_{CT}) resulting from the removal of the DNA reporter from the electrode surface upon the activation of Cas12a collateral activity (Bonini et al., 2021a). As a consequence, the CRISPR/Cas systems seem perfect candidates for the development of a new class of one-pot portable PoC devices (Phan et al., 2022), thanks to the potential coupling to isothermal amplification methods (L. Zhang et al., 2022) and the possibility to freeze-dry the Cas:crRNA complex (Arizti-Sanz et al., 2022). In particular, the integration of CRISPR technology into electrochemical devices is very promising for PoC devices. These systems are effective in complex sample matrices, require low-cost instrumentation, are easily scalable and offer multiplexing capabilities (Ambaye et al., 2021; Fernandes et al., 2020). The landscape of electrode fabrication has been transformed by inkjet printing technologies, outperforming traditional methods in terms of speed, cost-effectiveness and precision (Ambaye et al., 2021; Baek et al., 2022;
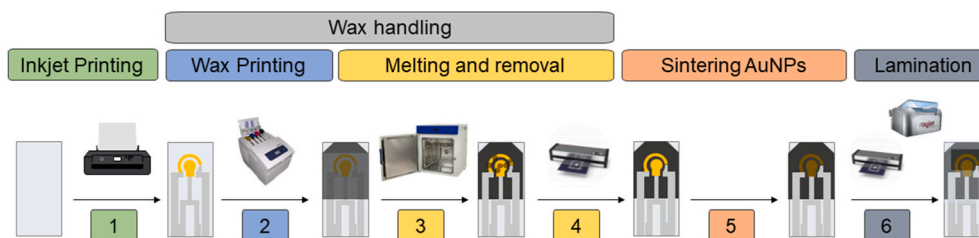
Fig. 2. *Workflow of Inkjet-Printed Electrode Fabrication. This schematic provides an overview of the sequential steps and essential instruments involved in the fabrication process of metal nanoparticle-based inkjet-printed electrodes.*

Grillo et al., 2022). In inkjet printing, a digital and non-contact process, specialised printers apply precise amounts of conductive ink to various substrates (Donie et al., 2021; Tagliaferri et al., 2021). This approach offers numerous advantages, such as the ability to produce intricate patterns with high resolution, the use of a wide range of nanomaterial-based inks and the flexibility to produce electrodes in large quantities with consistent reproducibility (Fukuda et al., 2013; Jarošová et al., 2019; Kim et al., 2023; Moya et al., 2017; Sundriyal and Bhattacharya, 2017).

Aiming at this goal, a new fabrication strategy using an office inkjet-printer and a gold nanoparticle (AuNP)-based ink was recently reported to produce low-cost and disposable nanostructured gold electrodes (Rosati et al., 2022; Urban et al., 2023; Rossetti et al., 2024). In the present study, these electrodes were functionalized with methylene-blue (MB)-labelled ssDNA reporters that would be digested upon triggering the Cas12a trans-activity in the presence of the target genome, specifically from *E. coli* and *S. aureus* strains. The mechanism of detection of the biosensor is schematized in Fig. 1B and explained in Section 3.1. The use of inkjet-printed electrodes simplifies the integration into a PoC device, as their design can be tailored to fit the characteristics of the sensing platform. Additionally, they serve as a valid and cost-effective alternative to commercial screen-printed electrodes. The inherent porosity resulting from the arrangement of the printed AuNPs results in a higher electroactive surface, leading to increased sensitivity. Throughout this study, we optimised the biosensing system on inkjet-printed electrodes and compared its performance with sensors fabricated by commercial screen-printed gold electrodes. The biosensor underwent successful testing on clinically isolated samples, showcasing its potential utility as a tool for developing a new class of low-cost and portable devices.

2. Materials and methods

2.1. Materials and reagents

For the fabrication of the inkjet-printed electrodes, the substrate (NB-TP-3GU100) and the AgNPs ink (NBSIJ-MU01) were purchased from Mitsubishi Paper Mills Silver NanoTM, while AuNPs dispersion for the preparation of custom made AuNPs based ink was purchased from RHP Technology Gmb. Metrohm DropSens C220BT (Metrohm, Switzerland) screen-printed (SP) gold electrodes were used for the comparison of properties with inkjet-printed (IP) nanostructured gold electrodes. Gold disk electrodes were purchased from eDAQ (Australia). Luria Bertani broth (LB, ThermoFisher Scientific, Waltham, Massachusetts, USA) and LB agar/broth (PanReac AppliChem GmbH, Darmstadt, Germany) were used for bacteria growth. PCR was performed using Dream Taq DNA polymerase (ThermoFisher Scientific, Waltham, Massachusetts, USA) and QIAquick PCR purification Kit (Qiagen, Venlo, Netherlands). All the lyophilized HPLC grade oligonucleotides were purchased from Biomers (Biomets.net GmbH, Germany). The gRNA sequences were purchased from ThermoFisher scientific (Waltham, Massachusetts, USA) and Biomers (Biomers.net GmbH, Germany). All the oligonucletodides were resuspended in nuclease free water. Tris (2-carboxyethyl)phosphine

(TCEP) and 6-mercapto-1-hexanol (MCH) were purchased from Sigma-Aldrich (USA). Assembling buffer (pH 7) was prepared using 10 mM PBS (Sigma-Aldrich, USA), 1 M NaCl (Sigma-Aldrich, USA), 1 mM MgCl$_2$ (Sigma-Aldrich, USA). LbaCas12a and 10x NEB were purchased from New England Biolabs (Ipswich, MA, USA). All the measurements were performed in NE Buffer (pH 7.9) (50 mM NaCl, 10 mM MgCl$_2$, 10 mM Tris-HCl), unless otherwise stated. NaCl, MgCl$_2$, Tris-HCl, KCl, Potassium ferricyanide (III) were purchased from Sigma-Aldrich, Spain and used without any further purifications. buffer (Sigma-Aldrich, USA).

2.2. Fabrication of the inkjet-printed gold electrodes

Inkjet-printed electrodes were produced using a porous commercial substrate (NB-TP-3GU100) in combination with a consumer inkjet printer, following previous work (Rosati et al., 2022). The choice of a porous substrate offers several advantages in terms of ink absorption, film formation, adhesion and stability, making it a suitable choice for the production of inkjet printed electrodes (Rosati et al., 2019a; 2019b, 2022; Rossetti et al., 2024). The characteristics of the substrate allow a straightforward printing of conductive silver films, as the inks instantly dry upon contact with the substrate and sintering of silver nanoparticles occurs at room temperature. As reported recently (Urban et al., 2023), the electrodes were inkjet-printed by an office printer (EPSON XP15000) loaded with refillable cartridges containing inks based on metal nanoparticles, namely AgNPs ink (NBSIJ-MU01) and a custom made AuNPs based ink, respectively (Fig. 2, **1**). The rheological parameters of the inks were investigated in the same work, and match the printability window of the selected printer. Then, a layer of wax (Fig. 2, **2**) and was printed on the top of the electrodes by a Xerox ColorCube 8580 and melted in an oven at 85 °C for 5 min. Thus, the wax penetrated into the porous matrix of the substrate, creating an insulating barrier that prevents the penetration of the solution into the substrate's pores, thus avoiding the formation of parasitic currents (Figs. 2, **3**). This operation was repeated twice and the excess wax over the film surface was eventually removed. More in detail, the waxed electrodes were covered with a piece of office paper and cleaned by passing them 8 times inside a hot laminator at slowest possible speed (Figs. 2, **4**). During lamination, the wax on the electrode surface melted and was absorbed in the paper by capillarity. AuNPs were then sintered using a novel approach that improves conductivity without compromising the nanostructure (Urban et al., 2023). While sintering of the AgNPs ink happens directly on the substrate, sintering of AuNPs occurs by immersing the cleaned device in a 1 M NaBH$_4$ solution for 10 min (Figs. 2, **5**). Subsequently, the devices were first rinsed by immersion in MilliQ water for 20 min, then dried with a stream of N$_2$ and finally at room temperature. A bi-adhesive plastic lamination card cut with a Rayjet Laser Cutter (power of 50, speed of 70, for two passes) was used to define the working area of the electrode. The electrodes were finally passed through a hot laminator to assemble and glue the different layers together (Figs. 2, **6**). The resulting device was about 3 cm in length, with a defined working electrode area of 11.7 mm^2.

2.3. Bacterial strains and genomic DNA extraction

Escherichia coli (*E. coli*) and *Staphylococcus aureus (S. aureus)* bacteria were used as targets for the Cas12a/gRNA system, and species-specific housekeeping genes were selected. In particular, malate dehydrogenase (*mdh*, GenBank GeneID: 947854) and thermonuclease (*nuc*, GenBank GeneID: 45574557) encoding genes were selected for *E. coli* and *S. aureus*, respectively.

The biosensor was developed studying Cas12a/gRNA activities on Gram-negative (*E. coli*, ATCC 25922) and Gram-positive (*S. aureus*, ATCC 6538) reference laboratory strains. Reference strains of these model organisms were purchased from the American Type Culture Collection (ATCC, Manassas, Virginia, USA). Clinical isolates were selected from a collection of bacterial strains stored at the Department of Biology, Microbiology section of the University of Pisa (see Table S1). All strains were stored at −80 °C in fresh Luria Bertani broth (LB) supplemented with 20% glycerol. When necessary, bacteria were grown on LB agar/broth at 37 °C overnight (ON). Genomic DNA extraction is described in section 1.1 of SI.

2.4. Gene selection and amplification

Primers were designed for the amplification by PCR of an internal region comprising the DNA sequence complementary to the gRNA, for the housekeeping genes *mdh* and *nuc* from *E. coli* and *S. aureus*, respectively (Table S2). The 99 bp-*mdh* and 150 bp-*nuc* gene fragments were amplified using the Dream Taq DNA polymerase. DreamTaq DNA polymerase (0.025 U/mL), dNTPs (0.2 mM), primers forward and reverse (0.2 μM) and DreamTaq buffer (1X) containing MgCl2 (2.5 mM), were reacted with 30 ng of genomic DNA. The amplification conditions were as follows: $T_{denaturation\_start}$ = 95 °C for 2 s; $T_{denaturation}$ = 95 °C for 30 s; $T_{annealing}$ = 52 °C for 30 s; $T_{elongation}$ = 72 °C for 10 s; number of cycles = 40; $T_{elongation\_final}$ = 72 °C, for 5'. Biodoc-H Imaging System transilluminator (Somatco, Riyadh, Saudi Arabia) was used in combination with the TS Software to visualise amplified fragments run in 2% agarose gel in TBE buffer. The QIAquick PCR purification Kit was used to purify the amplicons, while UV spectroscopy (BioPhotometer, Eppendorf) was used for quantification. The amplified DNA was stored at −20 °C in nuclease free water. Fig. S1 shows results of gel electrophoresis of the amplified fragments.

2.5. Oligonucleotides selection and design

2.5.1. ssDNA-MB reporter design

Three different ssDNA reporters were used: linear stick-ssDNA-MB, hairpin (hp) hp-ssDNA-MB-15loop and hp-ssDNA-MB-10 T-loop. Oligonucleotides were purchased already modified. An amino link C6 has been used for the conjugation. Specifically, a MB-NHS ester was introduced onto the DNA via coupling to an amine attached via a 6-carbon linker to the 3'-end, while thiol C6 modifier (OH–C6–S–S–C6) is linked in 5'. Reporters were designed and their stability checked by using an online software (NUPACK, https://www.nupack.org/). Oligonucleotides sequence and secondary structures are shown in the Supporting Information (SI), Table S3 and Fig. S2, respectively.

2.5.2. Design of the guide RNA (gRNA)

Guide RNA sequences were designed using SnapGene software, searching for the specific Protospacer Adjacent Motif (PAM) sequence (5' – TTTN– 3') within the sequence of each selected housekeeping gene. A 20-nucleotide sequence after the (PAM) was selected and added to the crRNA scaffold (see Table S4). Selected gRNA sequences were compared with an online tool (Eukaryotic Pathogen CRISPR Guide RNA/DNA Design Tool, EuPaGDT). The hybridized forms of the gRNA with the target DNA amplicons are shown in Table S5.

2.6. Operative parameters

2.6.1. Electrode cleaning and functionalization

Prior to functionalization, inkjet-printed electrodes were electrochemically cleaned by different cyclic voltammetry (CV) cycles in 0.5 M H_2SO_4. First, 30 cycles at scan rate 2 V/s and then 10 cycles at 0.1 V/s were found to be optimal to clean this kind of electrodes (Figs. S4A and S4B). Instead, screen-printed electrodes were cleaned by 50 cycles at a scan rate of 0.1 V/s in 0.5 M H_2SO_4. CV and electrochemical impedance spectroscopy (EIS) measurements in FC solution (prepared using 10 mM $[Fe(CN)_6]^{3/4-}$ and 10 mM KCl) before and after cleaning are compared in Figs. S4C and S4D and discussed in Section 3.2.1. The electroactive surface area of inkjet-printed electrodes was calculated by using the Randles-Sevcik equation and extrapolating data from different CVs in FC solution at different scan rates (0.01, 0.03, 0.06, 0.08, 0.1, 0.2, 0.3, 0.5 V/s), potential from −0.2 to 0.5 V (Khashaba et al., 2017). Roughness was calculated from the area of the oxygen reduction peak in CV in 0.05 M H_2SO_4, potential from −0.35 to 1.35 V, scan rate 0.1 V/s (Carvalhal et al., 2005). Measurements were recorded using an external Ag/AgCl (1 M KCl) reference electrode and a platinum counter electrode.

Functionalization was accomplished by forming a self-assembled monolayer (SAM) on the gold nanoparticles surface. The procedure followed the protocol described by Xiao et al. (2007). Briefly, the ssDNA-MB reporter was reduced using TCEP and then diluted in assembling buffer down to a concentration of 1 μM. The reporter solution was drop-casted on the WE surface and left in humid chamber at 4 °C. After 1 h, electrodes were washed and passivated with a solution 2 mM of MCH in assembling buffer ON. The same protocol was used for all but the hp reporters, which needed an additional annealing step to achieve the most stable conformation after thawing. CV and EIS were performed also after functionalization, and the relevant results are compared in Fig. S5 and discussed in Section 3.2.2. The same procedure was followed for both inkjet-printed and screen-printed electrodes.

#### 2.6.2. Probe surface density calculation

The probe surface density was calculated from the alternate current voltammetry (ACV) peak current (Ricci et al., 2007) by exploiting the presence of the MB redox probe on the ssDNA reporter. The relationship between the average peak current in a voltammogram $I_{avg}(E_0)$ and the probe surface density N_{tot}, i.e. the number of moles of electroactive DNA probe per electrode surface unit area, is shown in Equation (1):

$$I_{avg}(E_o) = 2nfFN_{tot}\frac{\sinh(nFE_{ac}/RT)}{\cosh(nFE_{ac}/RT)+1} \qquad (1)$$

where *n* is the number of electrons transferred per redox event (n = 2 for MB), *f* is the frequency of the applied AC voltage perturbation, *F* is the Faraday current, E_{ac} is the peak amplitude, *R* is the universal gas constant and *T* is the temperature. The average current peak was calculated at four different frequencies (5, 10, 50 and 100 Hz) to obtain a representative N_{tot} value. The mean probe density was calculated from N_{tot} using the apparent surface area (11.7 mm^2 for inkjet-printed electrodes used in this work). Alternating current voltammograms were recorded from −0.10 to −0.40 V vs Ag/AgCl (1 M KCl) reference electrode with a platinum counter electrode. The experiments were conducted in assembling buffer at 37 °C, using a 25 mV AC potential. PalmSens 4 (PalmSens BV, Netherlands) potentiostat and PSTrace 5.9 software (PalmSens BV, Netherlands) were used to record and manipulate the voltammograms.

Probe density results with inkjet-printed electrode ($\varnothing_{WE}$ = 4 mm) were compared to those reported for DropSens C220BT screen-printed gold electrodes ($\varnothing_{WE}$ = 4 mm) and gold disk electrodes ($\varnothing$ = 1 mm). Experiments on these electrodes were performed following the same procedure used for the inkjet-printed ones.
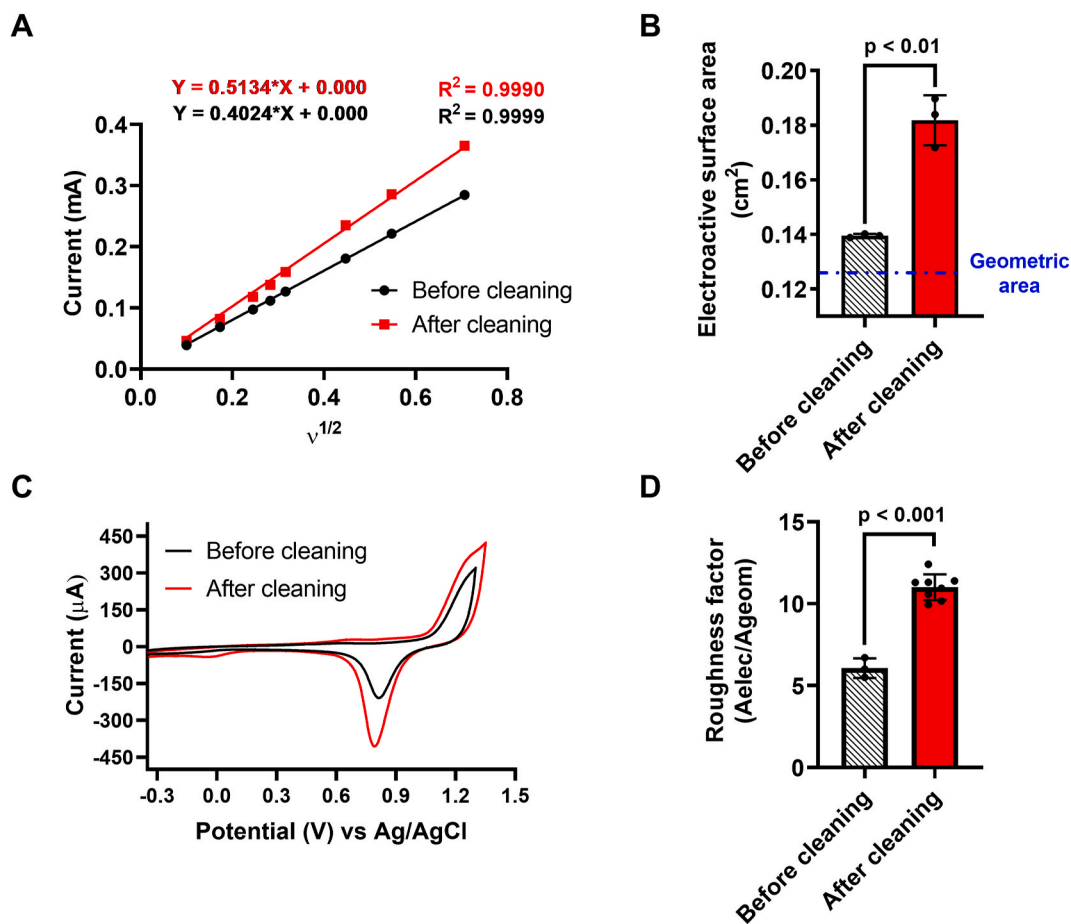
Fig. 3. *Electrochemical characterization of the bare inkjet-printed electrodes. (A) Linear correlation between oxidation CV peak current and the square root of scan rate. CV registered in FC solution, from -0.2 to 0.5 V, at different scan rates. (B) Electroactive area calculated by the Randles-Sevcik equation before and after cleaning, compared to geometric area. (C) CV in $0.05M\ H_2SO_4$, from -0.35 to 1.35 V, scan rate 0.1 V, before and after cleaning for roughness calculation. (D) Roughness values, calculated as the ratio between electroactive area and geometric area, before and after the cleaning treatment. All measurements were made in triplicate and the error bar indicates the standard deviation.*

2.6.3. Cas12a/gRNA complex assembly and activation

The activation of the Cas12a/gRNA complex was performed on *mdh*- and *nuc*-gene fragments amplified from *E. coli* and *S. aureus* genomic DNAs, respectively. The activation reactions were performed in 20 μL with a molar ratio LbaCas12a:gRNA:target of 10:10:1 (unless otherwise stated) in RNase-free water. The reactions were prepared as follows: 13.8 μL of RNase-free H_2O, 2 μL of 10X NEB 2.1, 2 μL of 1 μM LbaCas12a (final concentration 100 nM) and 2 μL of 1 μM gRNA (final concentration 100 nM). The Cas12a:gRNA complex was allowed to form for 30 min at 37 °C, then 2 μL of 100 nM target DNA (final concentration 10 nM) were added and the solution was incubated at 37 °C. After 30 min, the solution containing the activated Cas12a:gRNA duplex was moved on the surface of the working electrode and incubated for 1 h at 37 °C. The electrodes were then washed to make them ready for the measurement.

2.6.4. Square wave voltammetry Cas12a/gRNA investigation

Square wave voltammetry was performed to monitor the presence of methylene blue near the electrode surface (Tani et al., 2001). Voltammograms were recorded from −0.10 to −0.40 V. The experiments were conducted in NEBuffer at 37 °C, using a 25 mV amplitude, at a frequency of 90 Hz. Experiments on *mdh* and *nuc* amplicons were conducted using an external Ag/AgCl (1 M KCl) reference electrode and a platinum counter electrode, while those performed on clinical isolates samples were performed using the reference (AgNPs) and counter (AuNPs) electrodes printed directly on the chip. PalmSens 4 potentiostat and

PSTrace 5.9 software were used to record and manipulate the voltammograms. Measurements at 37 °C were performed placing the electrodes inside a lab incubator ICN 55 Plus (Argolab, Italy) set at that temperature.

3. Results and discussion

3.1. Assay biosensing principle

The activation of Cas12a enzyme and the biosensor detection mechanism are schematized in Fig. 1A and B, respectively. A rationally designed ssDNA reporter labelled with methylene blue (ssDNA-MB) is immobilised on the working electrode surface and its presence provides a large current signal by square wave voltammetry (SWV) due to the MB redox probe, which favours the electron exchange with the electrode. Upon the recognition of the DNA target sequence, and following binding of the CRISPR/Cas12a system, the *trans*-activity is triggered, leading to the cleavage of the ssDNA reporter. Consequently, the SWV signal associated with reduction of methylene blue decreases.

3.2. Biosensor characterization

3.2.1. Cleaning

The use of porous substrates like the one in this work, facilitates printing with consumer inkjet printers, thanks to fast drying and high adhesion of the metal nanoparticles inks. As previously demonstrated,
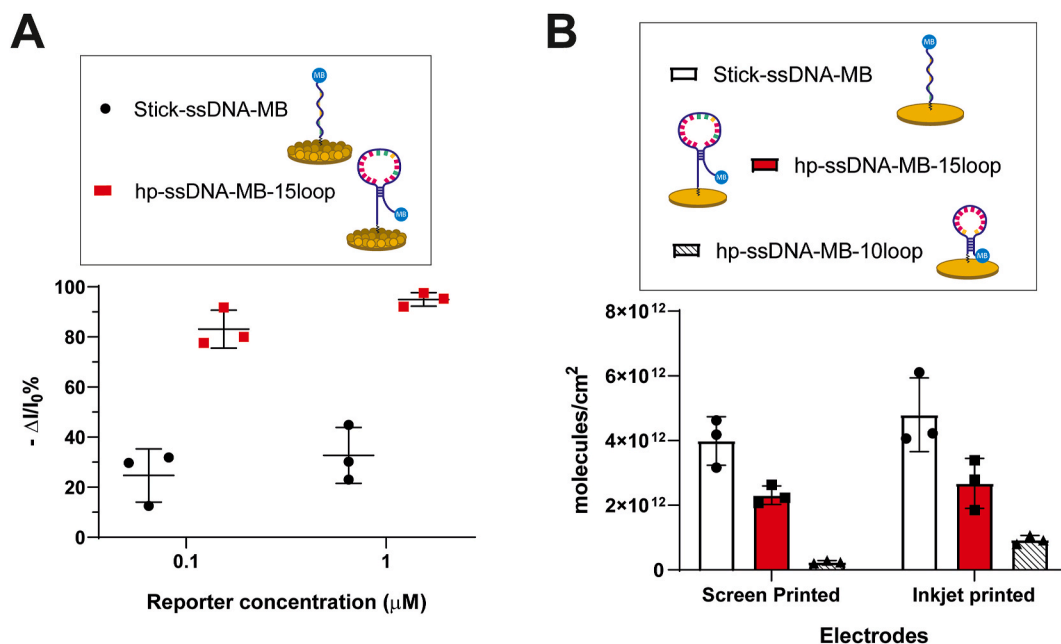
Fig. 4. *Sensor response and ssDNA probe density values for IP and SP electrodes:* (A) Signal decrease after detection of E. coli laboratory strain at different concentration of reporter on inkjet-printed (IP) electrodes. Higher current decrease was observed for 1 μM hp-ssDNA-MB-15loop reporter (red squares); experiments were performed in saturating conditions (Cas12a/gRNA:target 10:13, 1 h incubation). (B) Probe density values calculated for 1 μM stick-ssDNA-MB, 1 μM hp-ssDNA-MB-15loop and 1 μM hp-ssDNA-MB-10loop on both DropSens (SP) gold electrodes and IP gold electrodes. Error bars indicate the standard deviation (n = 3).

when the electrode is wet, a new element of the equivalent circuit is created and parasitic currents are running in the coating due to the water permeation. The wax mitigated this effect, by partially filling the substrate's coating, creating a dielectric barrier with high resistance impeding the current flow (Rosati et al., 2022). One of the most critical steps in the workflow of the fabrication of inkjet-printed electrodes then becomes the removal of the wax from the top of the waxed device. An incorrect removal would leave large chunks of wax on the electrode surface, and this would severely hinder the electrochemical properties as well as the correct sintering of gold nanoparticles. SEM characterization (data not shown) confirmed that the wax was correctly removed after 8 passages in the laminator without substantial leftover, which would appear as a blurry and reflective surface due to charging effects.

After the physical cleaning, the inkjet-printed working electrode surface was also electrochemically cleaned. As shown in Fig. S3, the electrode nanostructure did not change significantly after cleaning with sulfuric acid. The fast and effective cleaning protocol also activated the electrode surface, making it suitable for the immobilisation of a large amount of target. Figs. S4C and D shows the CV and EIS plots before and after cleaning. A slight increase of current and a negligible difference of distance between peaks ΔE (values before and after cleaning both about 100 ± 5 mV) were observed from CV, whereas the charge transfer resistance (R_{CT}) decreased from an initial average value of 87 ± 9 Ω to zero after cleaning. Cyclic voltammetry current peaks at different scan rates are plotted versus the square root of the scan rate in Fig. 3A, which shows an increased value of slope after the cleaning process. This parameter is correlated to the effective electrode surface area from the Randles-Sevick equation (Khashaba et al., 2017). The electroactive surface area calculated before and after cleaning is compared to the geometric area in Fig. 3B. A remarkable increase was observed after cleaning, as the oxygen reduction peak, correlated to the electroactive area, increased to 59 ± 2 μAV from an initial value of 33.4 ± 0.9 μAV (28% increase). Fig. 3C reports CV scan in 0.05 M H_2SO_4 before and after cleaning. The electroactive area was obtained by dividing the area of the oxygen reduction peak by the scan rate (0.1 V/s) and then dividing the resulting value by 390 μC/cm^2 (that represents the charge required to reduce the chemisorbed oxygen on gold surface in that buffer at that

scan rate) (Carvalhal et al., 2005). The roughness factor was then calculated as the ratio between electroactive area and geometrical area. Values are shown in Fig. 3D. The roughness factor calculated for inkjet-printed electrodes, about 12.1 ± 0.6, was also compared to values calculated for screen-printed gold electrodes (DropSens) and gold disk electrodes, approximately 2.3 and 1.2, respectively (Bonini et al., 2021a; Zamani et al., 2022). This higher value could be attributed to their distinct fabrication processes and to the chemical sintering method (Urban et al., 2023).

3.2.2. Functionalization of the electrodes

CV and EIS plots performed before and after functionalizing inkjet-printed electrodes with a linear reporter (stick-ssDNA-MB) were compared. Fig. S5A shows CV scans in FC solution reporting an increase of 77 ± 5 mV of ΔE_p and decrease in current peaks of about 123 ± 11 μA that suggest the formation of a self-assembled monolayer, whereas an increase of the R_{CT} (400 ± 15 Ω) in the Nyquist plot registered during the EIS analysis in the same solution can be seen in Fig. S5B that leads to the same conclusion (Bonini et al., 2021a) (average values calculated for 3 electrodes). Fig. S5C reports the SWV peak of MB at 90 Hz and 37 °C measured in NEB, while Fig. S5D shows the change in current peak of MB for different concentrations of functionalized stick-ssDNA-MB. These results confirm the effective functionalization and activation of the electrode surface after the cleaning process. The functionalization of the electrode surface was also observed when employing other ssDNA reporters (Fig. S5E). The presence and stability of the ssDNA reporter on the electrode surface are crucial for these turn-off biosensors. For instance, Fig. S6A demonstrates the stability of the reporter, assessed by recording square wave voltammograms every 12 min over 3 h, during which the methylene blue (MB) peak remained constant. The drying step using a gentle nitrogen flow was identified as a critical point in the procedure, as a significant decrease in MB current intensity occurred after this step (Fig. S6B). Consequently, no drying was performed between measurements.

### 3.2.3. Probe density calculation

Probe densities for different electrodes and reporters were calculated
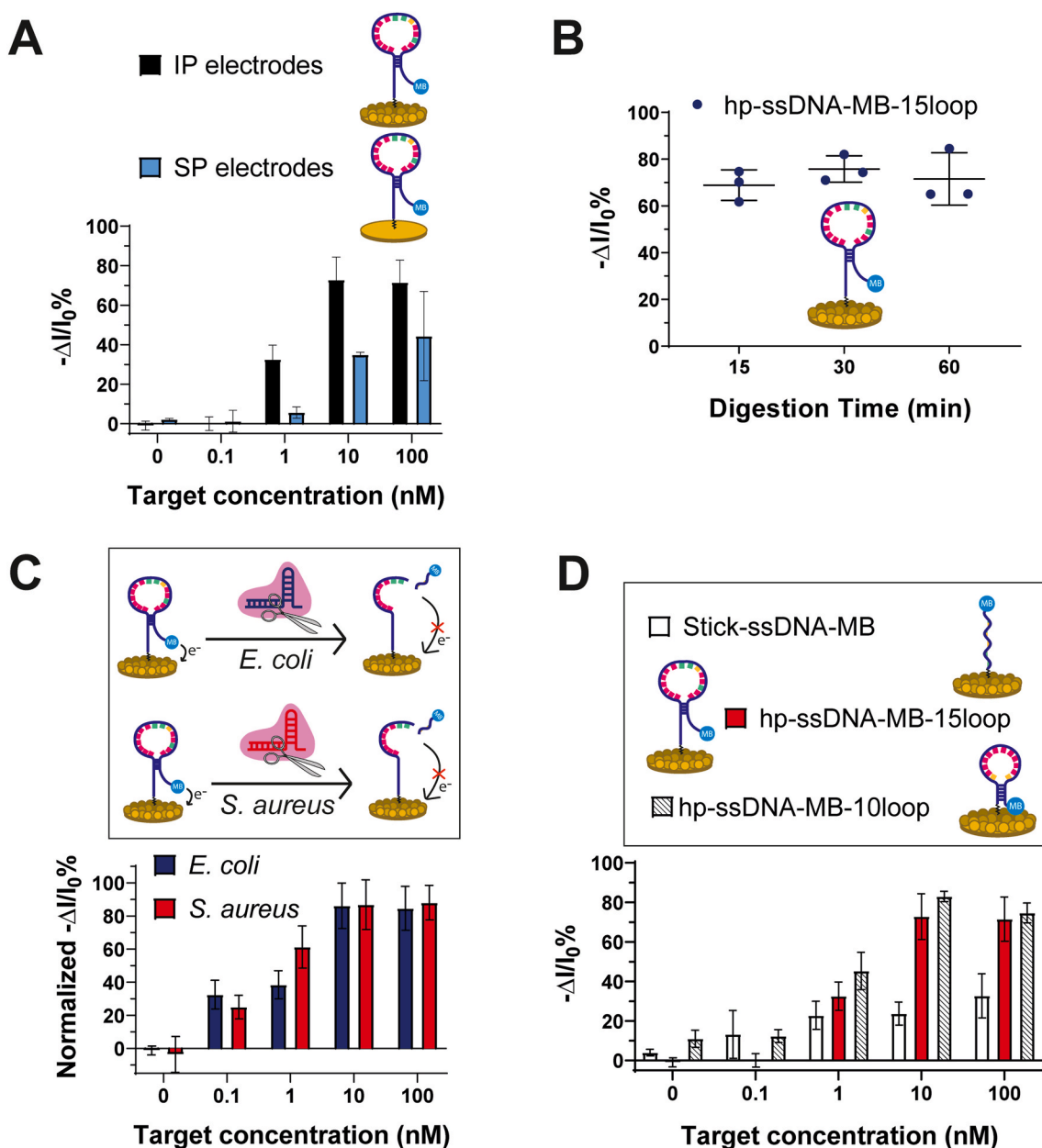
Fig. 5. *Biosensor response at different target concentrations. All measurements were performed in triplicate after a 1 h long trans-activity cleavage by activated Cas12a/ gRNA (error bars indicate the standard deviation): (A) Calibration with E. coli laboratory strain of sensors fabricated with inkjet-printed and screen-printed electrodes and 1 μM solution of hp-ssDNA-MB-15loop reporter. (B) Signals decrease at different times after detection of E. coli laboratory strain from sensors fabricated with inkjet-printed electrodes and 1 μM solution of hp-ssDNA-MB-15loop reporter. (C) Normalised data of E. coli and S. aureus laboratory strains of sensors fabricated with inkjet-printed electrodes and 1 μM solution of hp-ssDNA-MB-15loop reporter. (D) Calibration with E. coli laboratory strain of sensors fabricated with inkjet-printed electrodes and 1 μM stick-ssDNA-MB, hp-ssDNA-MB-15loop and hp-ssDNA-MB-10loop reporters.*

using Equation (1) (Section 2.6.2) to quantify the amount of reporter on the electrode surface. Screen-printed gold electrodes were functionalized with stick-ssDNA-MB and hp-ssDNA-MB-15loop reporter at two different concentrations (0.1 and 1 μM) (Fig. S7A). Higher probe densities were observed for the linear ((7.6 ± 0.7)·10^{11} molecules cm^{-2} and (4.0 ± 0.4)·10^{12} molecules cm^{-2} for 0.1 and 1 μM of reporter, respectively) than for the hairpin reporter ((5.5 ± 0.6)·10^{11} molecules cm^{-2} and (2.3 ± 0.2)·10^{12} molecules cm^{-2} for 0.1 and 1 μM of reporter, respectively). This difference could result from a denser packing of the former during the formation of the SAM owing to its smaller steric hindrance (Biagiotti et al., 2012). Additionally, a noticeable increase in the number of molecules was observed when the higher concentration of reporter was used (1 μM rather than 0.1 μM). Since no improvement in

performance (signal decrease percentage after Cas12a/gRNA digestion) was observed for the lower concentration of reporter (Fig. 4A), we decided to functionalize the electrodes using a reporter concentration of 1 μM to take advantage of the higher current intensity. Moreover, probe density values for three different reporters (1 μM) on both inkjet-printed and screen-printed electrodes are reported in Fig. 4B. A larger number of reporter molecules on the electrode surface was calculated for the stick-ssDNA-MB than for hp-ssDNA-MB-15loop and hp-ssDNA-MB-10loop. We speculate that hairpin structures take up more surface area per molecule due to their folded configuration, which means that fewer molecules can attach overall (Ricci et al., 2007; Cederquist and Keating, 2010). This trend was consistent for both inkjet-printed and screen-printed electrodes, with higher values for
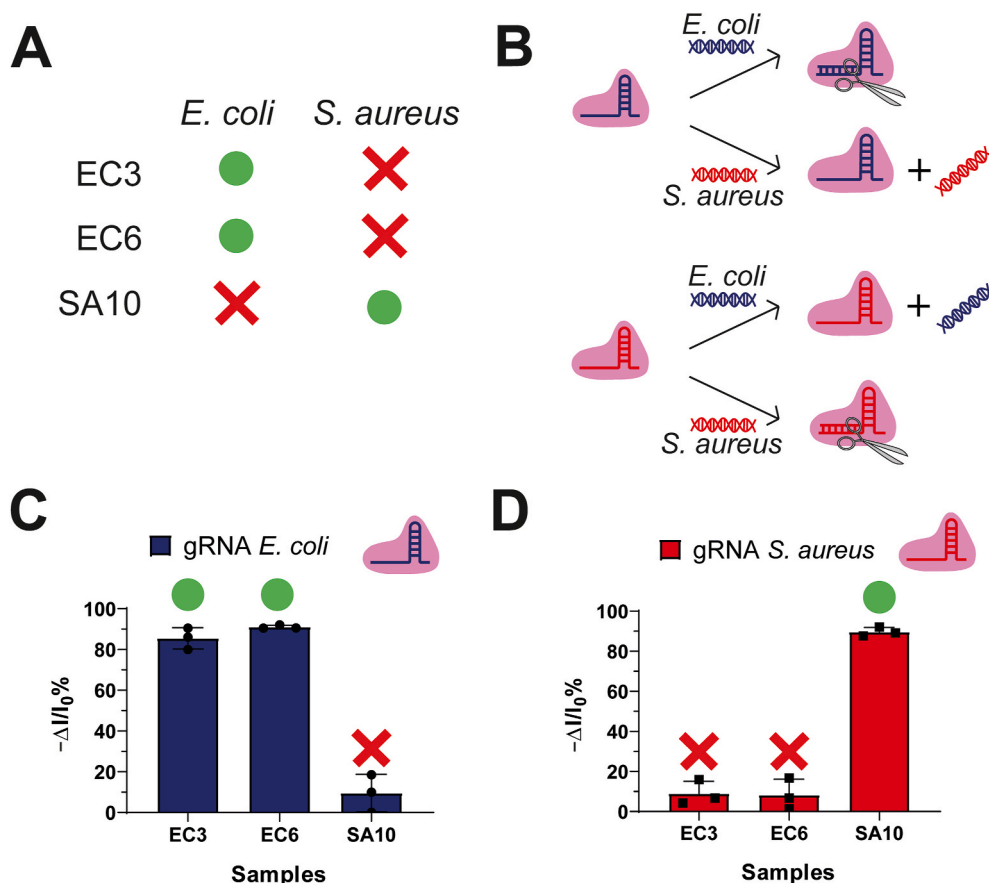
Fig. 6. *Biosensor response for clinical isolates samples and specificity.* Signal decrease after detection of E. coli and S. aureus clinical isolate samples (10 nM dsDNA target) by sensors using inkjet-printed electrodes and 1 μM solution of hp-ssDNA-MB-10loop reporter. Specificity was investigated by swapping gRNA and target bacteria. (A) Bacteria species for each sample (EC3, EC6, SA10); (B) Cas12a/gRNA activation occurs only when the target dsDNA strain, complementary to the designed gRNA, is detected: E. coli gRNA (blue) forms the duplex only with the target sequence from E. coli genomic (blue), while inactivation occurs in presence of S. aureus dsDNA (red). (C) Signal decrease values registered after detection of clinical isolates samples using E. coli gRNA. Activation occurs only for samples containing E. coli target sequence (EC3, EC6). (D) Signal decrease values registered after detection of clinical isolates samples using S. aureus gRNA. Activation occurs only for samples containing S. aureus target sequence (SA10).

inkjet-printed owing to the larger electroactive area available (for screen-printed: stick-ssDNA-MB $(4.0 \pm 0.4)\cdot10^{12}$ molecules cm^{-2}, hp-ssDNA-MB-15loop $(2.3 \pm 0.2)\cdot10^{12}$ molecules cm^{-2}, hp-ssDNA-MB-10loop $(2.4 \pm 0.3)\cdot10^{11}$ molecules cm^{-2}; for inkjet-printed: stick-ssDNA-MB $(4.8 \pm 0.7)\cdot10^{12}$ molecules cm^{-2}, hp-ssDNA-MB-15loop $(2.7 \pm 0.4)\cdot10^{12}$ molecules cm^{-2}, hp-ssDNA-MB-10loop $(9.3 \pm 0.8)\cdot10^{11}$ molecules cm^{-2}). Probe density values for 1 μM hp-ssDNA-MB-15loop were calculated for gold disk electrodes as well (Fig. S7B). As expected, because of the small electroactive area, gold disk electrodes exhibited the lowest number of molecules $((5.6 \pm 1.2)\cdot10^{11}$ molecules $cm^{-2})$ compared to the other electrodes. Probe density values are resumed in Table S6.

3.3. Cas12a gRNA biosensing assay performances

3.3.1. Performances of different sensors for DNA detection

Biosensor performances were initially assessed and optimised for the *mdh* target DNA (99 bp) amplified by PCR from *E. coli* (ATCC, 25922). Fig. 5A shows calibration curves of sensors fabricated with both inkjet-printed and screen-printed electrodes and functionalized with hp-ssDNA-MB-15loop. Sensors fabricated with inkjet-printed electrodes exhibited a better sensitivity than those using screen-printed electrodes. Responses at different times from sensors based on inkjet-printed electrodes functionalized with a 1 μM solution of hp-ssDNA-MB-15loop reporter are shown in Fig. 5B. The substantial signal decrease after only 15 min suggests the possibility of reducing the biosensor's analysis time.

The experimental procedure used for the detection of *E. coli mdh* amplicon was similarly applied to the detection of the *nuc* gene amplified from *S. aureus*. A notable feature of the CRISPR/Cas system is its programmability. Hence, we believed it crucial to demonstrate that a system designed and optimised for *E. coli* could effectively detect a completely different bacterium by simply changing the specifically designed gRNA. The new sensor calibration is reported in Fig. S8. Although sensitivity was slightly reduced for *S. aureus* compared to *E. coli*, the activation of the enzyme was correctly achieved. As enlightened in Fig. 5C, normalised curves from both pathogens, detected using inkjet-printed sensors, share a similar trend. To further improve sensor performances, a new hairpin reporter was tested. Literature highlighted the significant role of the reporter structure in determining the interaction with the Cas12a enzyme and the high affinity between its catalytic domains and the hairpin structure containing 10-thymine loop (hp-ssDNA-MB-10loop) (Rossetti et al., 2022). The hp-ssDNA-MB-10loop was used to functionalize both inkjet-printed and screen-printed electrodes. Calibration curves are shown in Fig. S9, and better results were achieved by the sensor fabricated using inkjet-printed electrodes. Moreover, Fig. 5D shows calibration plots of sensors fabricated with inkjet-printed electrodes and functionalized with 1 μM solutions of the three different reporters (signal decrease measured after 1-h long Cas12a/gRNA trans-activity). Hairpin reporters, particularly the hp-ssDNA-MB-10loop, provided a better sensitivity than the linear stick-ssDNA-MB reporter. We speculate that such difference may result from a smaller steric hindrance of linear reporters, which are

expected to form a more densely packed SAM hindering the enzyme penetration and the reporter cleavage. In contrast, hairpin reporters should be more easily accessible (Biagiotti et al., 2012; Deng et al., 2019; D. Zhang et al., 2020). This hypothesis is supported by the larger probe density of linear reporters than hairpin reporters obtained with the same concentration of functionalizing solution and electrode surface area. Then, hp-ssDNA-MB-10loop elicited larger responses than the hp-ssDNA-MB-15loop. This is consistent with literature (Rossetti et al., 2022), since the RuvC domain in Cas12a has a greater affinity for the poly-T chain present in the loop of the hp-ssDNA-MB-10loop reporter. However, since both enzyme and reporter were free in solution in Rossetti's study, we had no certainty that the same would apply with the reporter bound to the electrode surface. Therefore, higher sensitivities were obtained with sensors using inkjet-printed electrodes and either hp-ssDNA-MB-15loop or hp-ssDNA-MB-10loop reporters, for which a greater signal decrease was observed.

3.3.2. Detection of clinical isolates

The biosensor was subsequently employed for the detection of clinical isolates samples (Section 2.3 and Table S1). This is utterly important to demonstrate a possible practical use of this technology, as clinical isolates of the same species could be quite different from one another and from reference commercial strains. In this case, sensors fabricated with inkjet-printed electrodes and 1 μM solution of hp-ssDNA-MB-10loop reporter was utilized for the best performance during the optimization step (section 3.3.1). Clinical isolates were diluted with a Cas12a/gRNA:target ratio of 10:1 (target concentration of 10 nM), then response time was set at 1 h. EC3 and EC6 were detected using the gRNA designed for *E. coli*, while SA10 was detected using the gRNA designed for *S. aureus*. Enzyme activation was successfully achieved for all the targets, resulting in a substantial signal decrease of approximately 80–90%. Furthermore, the specificity of the Cas12a/gRNA system was investigated by swapping gRNA and target bacteria. When the *E. coli* gRNA was applied to detect *S. aureus* (and vice versa), the activation of the Cas12a/gRNA complex did not occur, and signal variations comparable to blank (absence of target in solution) were registered (Fig. 6).

4. Conclusions

In conclusion, we successfully developed and implemented a CRISPR/Cas-based electrochemical sensing device for pathogen detection utilising lab-made inkjet-printed electrodes. Our comparative analysis with commercial screen-printed electrodes showed that with the inkjet-printed electrode we obtain an enhanced signal intensity owing to its nanostructured surface and resulting in a higher electroactive area (Fig. S10). The biosensor's validation was accomplished with reference laboratory strains of Gram-negative *E. coli* and Gram-positive *S. aureus*, as well as clinical isolate samples. The optimization involved the use of various concentrations and types of ssDNA reporters, including harpin and linear variants, along with varying response times. Notably, the inkjet-printed electrodes utilising hp-ssDNA-MB-10loop reporters outperformed commercial screen-printed electrodes.

CRediT authorship contribution statement

Angela Gilda Carota: Writing – original draft, Visualization, Validation, Investigation, Formal analysis. **Andrea Bonini:** Writing – review & editing, Visualization, Methodology, Investigation. **Massimo Urban:** Writing – review & editing, Methodology, Investigation. **Noemi Poma:** Writing – review & editing, Methodology, Investigation. **Federico Maria Vivaldi:** Writing – review & editing, Visualization. **Arianna Tavanti:** Writing – review & editing, Supervision. **Marianna Rossetti:** Writing – review & editing, Visualization, Conceptualization. **Giulio Rosati:** Writing – review & editing, Supervision, Resources, Conceptualization. **Arben Merkoçi:** Supervision, Resources, Project administration, Funding acquisition. **Fabio Di Francesco:** Writing – review &

editing, Supervision, Resources, Project administration, Funding acquisition.

Declaration of competing interest

The authors declare that they have no known competing financial interests or personal relationships that could have appeared to influence the work reported in this paper.

Data availability

Data will be made available on request.

Acknowledgements

Appendix A. Supplementary data

Supplementary data to this article can be found online at https://doi.org/10.1016/j.bios.2024.116340.

References

Aman, R., Mahas, A., Mahfouz, M., 2020. Nucleic acid detection using CRISPR/Cas biosensing technologies. ACS Synth. Biol. 9 (6), 1226–1233. https://doi.org/10.1021/ACSSYNBIO.9B00507/ASSET/IMAGES/LARGE/SB9B00507_0004.JPEG.

Ambaye, A.D., Kefeni, K.K., Mishra, S.B., Nxumalo, E.N., Ntsendwana, B., 2021. Recent developments in nanotechnology-based printing electrode systems for electrochemical sensors. Talanta 225, 121951. https://doi.org/10.1016/J.TALANTA.2020.121951.

Amitai, G., Sorek, R., 2016. CRISPR–Cas adaptation: insights into the mechanism of action. Nat. Rev. Microbiol. 14 (2), 67–76. https://doi.org/10.1038/nrmicro.2015.14, 2016 14:2.

Arizti-Sanz, J., Bradley, A., Zhang, Y.B., Boehm, C.K., Freije, C.A., Grunberg, M.E., Kosoko-Thoroddsen, T.-S.F., Welch, N.L., Pillai, P.P., Mantena, S., 2022. Simplified Cas13-based assays for the fast identification of SARS-CoV-2 and its variants. Nat. Biomed. Eng. 6 (8), 932–943.

Baek, G.W., Kim, Y.J., Lee, M., Kwon, Y., Chun, B., Park, G., Seo, H., Yang, H., Kwak, J., 2022. Progress in the development of Active-matrix Quantum-dot light-emitting diodes driven by non-Si thin-film transistors. Materials 15 (23), 8511. https://doi.org/10.3390/MA15238511, 2022, Vol. 15, Page 8511.

Barenfanger, J., Drake, C., Kacich, G., 1999. Clinical and financial benefits of rapid bacterial identification and antimicrobial susceptibility testing. J. Clin. Microbiol. 37 (5), 1415–1418. https://doi.org/10.1128/JCM.37.5.1415-1418.1999/ASSET/

2149488A-65BA-4C72-8FFD-397F49AC82D2/ASSETS/GRAPHIC/JM0591344001.JPEG.

Biagiotti, V., Porchetta, A., Desiderati, S., Plaxco, K.W., Palleschi, G., Ricci, F., 2012. Probe accessibility effects on the performance of electrochemical biosensors employing DNA monolayers. Anal. Bioanal. Chem. 402 (1), 413–421. https://doi.org/10.1007/S00216-011-5361-0/FIGURES/6.

Bonini, A., Poma, N., Vivaldi, F., Biagini, D., Bottai, D., Tavanti, A., Di Francesco, F., 2021a. A label-free impedance biosensing assay based on CRISPR/Cas12a collateral activity for bacterial DNA detection. J. Pharmaceut. Biomed. Anal. 204, 114268.

Bonini, A., Poma, N., Vivaldi, F., Kirchhain, A., Salvo, P., Bottai, D., Tavanti, A., Di Francesco, F., 2021b. Advances in biosensing: the CRISPR/Cas system as a new powerful tool for the detection of nucleic acids. J. Pharmaceut. Biomed. Anal. 192, 113645 https://doi.org/10.1016/J.JPBA.2020.113645.

Bonini, A., Carota, A.G., Poma, N., Vivaldi, F.M., Biagini, D., Bottai, D., Lenzi, A., Tavanti, A., Di Francesco, F., Lomonaco, T., 2022. Emerging biosensing technologies towards early sepsis diagnosis and management. Biosensors 12 (10), 894. https://doi.org/10.3390/BIOS12100894, 2022, Vol. 12, Page 894.

Carvalhal, R.F., Freire, R.S., Kubota, L.T., 2005. Polycrystalline gold electrodes: a comparative study of pretreatment procedures used for cleaning and thiol self-assembly monolayer formation. Electroanalysis 17 (14), 1251–1259. https://doi.org/10.1002/ELAN.200403224.

Cederquist, K.B., Keating, C.D., 2010. Hybridization efficiency of molecular beacons bound to gold nanowires: effect of surface coverage and target length. Langmuir 26 (23), 18273–18280.

Cesewski, E., Johnson, B.N., 2020. Electrochemical biosensors for pathogen detection. Biosens. Bioelectron. 159, 112214.

Chen, J.S., Ma, E., Harrington, L.B., Da Costa, M., Tian, X., Palefsky, J.M., Doudna, J.A., 2018. CRISPR-Cas12a target binding unleashes indiscriminate single-stranded DNase activity. Science 360 (6387), 436–439.

Cheng, X., Li, Y., Kou, J., Liao, D., Zhang, W., Yin, L., Man, S., Ma, L., 2022. Novel non-nucleic acid targets detection strategies based on CRISPR/Cas toolboxes: a review. Biosens. Bioelectron. 215, 114559 https://doi.org/10.1016/J.BIOS.2022.114559.

Dai, Y., Somoza, R.A., Wang, L., Welter, J.F., Li, Y., Caplan, A.I., Liu, C.C., 2019. Exploring the trans-cleavage activity of CRISPR-Cas12a (cpf1) for the development of a universal electrochemical biosensor. Angew. Chem. 131 (48), 17560–17566.

Deng, M., Li, M., Li, F., Mao, X., Li, Q., Shen, J., Fan, C., Zuo, X., 2019. Programming accessibility of DNA monolayers for degradation-free whole-blood biosensors. ACS Mater. Lett. 1 (6), 671–676.

Donie, Y.J., Schlisske, S., Siddique, R.H., Mertens, A., Narasimhan, V., Schackmar, F., Pietsch, M., Hossain, I.M., Hernandez-Sosa, G., Lemmer, U., Gomard, G., 2021. Phase-separated nanophotonic structures by inkjet printing. ACS Nano 15 (4), 7305–7317.

Douterelo, I., Boxall, J.B., Deines, P., Sekar, R., Fish, K.E., Biggs, C.A., 2014. Methodological approaches for studying the microbial ecology of drinking water distribution systems. Water Res. 65, 134–156. https://doi.org/10.1016/J.WATRES.2014.07.008.

Fernandes, I.J., Aroche, A.F., Schuck, A., Lamberty, P., Peter, C.R., Hasenkamp, W., Rocha, T.L.A.C., 2020. Silver nanoparticle conductive inks: synthesis, characterization, and fabrication of inkjet-printed flexible electrodes. Sci. Rep. 10 (1), 1–11. https://doi.org/10.1038/s41598-020-65698-3, 2020 10:1.

Ferone, M., Gowen, A., Fanning, S., Scannell, A.G.M., 2020. Microbial detection and identification methods: bench top assays to omics approaches. Compr. Rev. Food Sci. Food Saf. 19 (6), 3106–3129.

Fukuda, K., Sekine, T., Kumaki, D., Tokito, S., 2013. Profile control of inkjet printed silver electrodes and their application to organic transistors. ACS Appl. Mater. Interfaces 5 (9), 3916–3920. https://doi.org/10.1021/AM400632S/ASSET/IMAGES/AM-2013-00632S_M003.GIF.

Gootenberg, J.S., Abudayyeh, O.O., Lee, J.W., Essletzbichler, P., Dy, A.J., Joung, J., Verdine, V., Donghia, N., Daringer, N.M., Freije, C.A., Myhrvold, C., Bhattacharyya, R.P., Livny, J., Regev, A., Koonin, E.V., Hung, D.T., Sabeti, P.C., Collins, J.J., Zhang, F., 2017. Nucleic acid detection with CRISPR-Cas13a/C2c2. Science 356 (6336), 438–442. https://doi.org/10.1126/SCIENCE.AAM9321/SUPPL_FILE/PAPV2.PDF.

Granados-Riveron, J.T., Aquino-Jarquin, G., Malpeli, G., Taguchi, Y.-H., 2021. CRISPR/Cas13-Based approaches for ultrasensitive and specific detection of microRNAs. Cells 10 (7), 1655. https://doi.org/10.3390/CELLS10071655, 2021, Vol. 10, Page 1655.

Grillo, A., Peng, Z., Pelella, A., Di Bartolomeo, A., Casiraghi, C., 2022. Etch and print: graphene-based diodes for silicon technology. ACS Nano. https://doi.org/10.1021/ACSNANO.2C10684/ASSET/IMAGES/LARGE/NN2C10684_0005.JPEG.

Ikuta, K.S., Swetschinski, L.R., Robles Aguilar, G., Sharara, F., Mestrovic, T., Gray, A.P., Davis Weaver, N., Wool, E.E., Han, C., Gershberg Hayoon, A., Aali, A., Mekonnen Abate, S., Abbasi-Kangevari, M., Abbasi-Kangevari, Z., Abd-Elsalam, S., Abebe, G., Abedi, A., Parsa Abhari, A., Abidi, H., et al., 2022. Global mortality associated with 33 bacterial pathogens in 2019: a systematic analysis for the Global Burden of Disease Study 2019. Lancet 400, 2221–2248. https://doi.org/10.1016/S0140-6736(22)02185-7.

Jarošová, R., McClure, S.E., Gajda, M., Jović, M., Girault, H.H., Lesch, A., Maiden, M., Waters, C., Swain, G.M., 2019. Inkjet-printed carbon nanotube electrodes for measuring pyocyanin and uric acid in a wound fluid simulant and culture media. Anal. Chem. 91 (14), 8835–8844. https://doi.org/10.1021/ACS.ANALCHEM.8B05591/ASSET/IMAGES/LARGE/AC-2018-05591A_0010.JPEG.

Jinek, M., Chylinski, K., Fonfara, I., Hauer, M., Doudna, J.A., Charpentier, E., 2012. A programmable dual-RNA-guided DNA endonuclease in adaptive bacterial immunity. Science 337 (6096), 816–821. https://doi.org/10.1126/SCIENCE.1225829/SUPPL_FILE/JINEK.SM.PDF.

Kharismasari, Yudin, Irkham, C., Zein, M.I.H.L., Hardianto, A., Nur Zakiyyah, S., Umar Ibrahim, A., Ozsoz, M., Wahyuni Hartati, Y., 2024. CRISPR/Cas12-based electrochemical biosensors for clinical diagnostic and food monitoring. Bioelectrochemistry 155, 108600. https://doi.org/10.1016/J.BIOELECHEM.2023.108600.

Khashaba, P.Y., Ali, H.R.H., El-Wekil, M.M., 2017. Highly sensitive and selective complexation based voltammetric methods for the analysis of rabeprazole sodium in real samples. RSC Adv. 7 (6), 3043–3050. https://doi.org/10.1039/C6RA25565E.

Ki, J., Na, H.-K., Yoon, S.W., Le, V.P., Lee, T.G., Lim, E.-K., 2022. CRISPR/Cas-Assisted colorimetric biosensor for point-of-use testing for african swine fever virus. ACS Sens. 7 (12), 3940–3946.

Kim, S.J., Choi, E., Won, D.Y., Han, G., An, K., Kang, K.T., Kim, S., 2023. Accelerated deep-learning-based process monitoring of microfluidic inkjet printing. CIRP Journal of Manufacturing Science and Technology 46, 65–73. https://doi.org/10.1016/J.CIRPJ.2023.07.010.

Land, K.J., Boeras, D.I., Chen, X.S., Ramsay, A.R., Peeling, R.W., 2018. REASSURED diagnostics to inform disease control strategies, strengthen health systems and improve patient outcomes. Nat. Microbiol. 4 (1), 46–54. https://doi.org/10.1038/s41564-018-0295-3.

Li, Y., Li, S., Wang, J., Liu, G., 2019. CRISPR/Cas systems towards next-generation biosensing. Trends Biotechnol. 37 (7), 730–743. https://doi.org/10.1016/j.tibtech.2018.12.005.

Ma, J., Li, X., Lou, C., Lin, X., Zhang, Z., Chen, D., Yang, S., 2023. Utility of CRISPR/Cas mediated electrochemical biosensors. Anal. Methods 15, 3785–3801.

Mao, Z., Chen, R., Wang, X., Zhou, Z., Peng, Y., Li, S., Han, D., Li, S., Wang, Y., Han, T., Liang, J., Ren, S., Gao, Z., 2022. CRISPR/Cas12a-based technology: a powerful tool for biosensing in food safety. Trends Food Sci. Technol. 122, 211–222. https://doi.org/10.1016/J.TIFS.2022.02.030.

Moya, A., Gabriel, G., Villa, R., Javier del Campo, F., 2017. Inkjet-printed electrochemical sensors. Curr. Opin. Electrochem. 3 (1), 29–39. https://doi.org/10.1016/J.COELEC.2017.05.003.

Mukama, O., Wu, J., Li, Z., Liang, Q., Yi, Z., Lu, X., Liu, Y., Liu, Y., Hussain, M., Makafe, G.G., Liu, J., Xu, N., Zeng, L., 2020. An ultrasensitive and specific point-of-care CRISPR/Cas12 based lateral flow biosensor for the rapid detection of nucleic acids. Biosens. Bioelectron. 159, 112143 https://doi.org/10.1016/J.BIOS.2020.112143.

Patterson, A.G., Yevstigneyeva, M.S., Fineran, P.C., 2017. Regulation of CRISPR–Cas adaptive immune systems. Curr. Opin. Microbiol. 37, 1–7. https://doi.org/10.1016/J.MIB.2017.02.004.

Phan, Q.A., Truong, L.B., Medina-Cruz, D., Dincer, C., Mostafavi, E., 2022. CRISPR/Cas-powered nanobiosensors for diagnostics. Biosens. Bioelectron. 197, 113732.

Rajapaksha, P., Elbourne, A., Gangadoo, S., Brown, R., Cozzolino, D., Chapman, J., 2019. A review of methods for the detection of pathogenic microorganisms. Analyst 144 (2), 396–411. https://doi.org/10.1039/C8AN01488D.

Rath, D., Amlinger, L., Rath, A., Lundgren, M., 2015. The CRISPR-Cas immune system: Biology, mechanisms and applications. Biochimie 117, 119–128. https://doi.org/10.1016/J.BIOCHI.2015.03.025.

Ricci, F., Lai, R.Y., Heeger, A.J., Plaxco, K.W., Sumner, J.J., 2007. Effect of molecular crowding on the response of an electrochemical DNA sensor. Langmuir 23 (12), 6827–6834. https://doi.org/10.1021/LA700328R/ASSET/IMAGES/MEDIUM/LA700328RN00001.GIF.

Rosati, G., Ravarotto, M., Sanavia, M., Scaramuzza, M., De Toni, A., Paccagnella, A., 2019a. Inkjet sensors produced by consumer printers with smartphone impedance readout. Sensing and Bio-Sensing Research 26, 100308. https://doi.org/10.1016/j.sbsr.2019.100308.

Rosati, G., Ravarotto, M., Scaramuzza, M., De Toni, A., Paccagnella, A., 2019b. Silver nanoparticles inkjet-printed flexible biosensor for rapid label-free antibiotic detection in milk. Sensor. Actuator. B Chem. 280, 280–289. https://doi.org/10.1016/j.snb.2018.09.084.

Rosati, G., Urban, M., Zhao, L., Yang, Q., e Silva, C. de C.C., Bonaldo, S., Parolo, C., Nguyen, E.P., Ortega, G., Fornasiero, P., 2022. A plug, print & play inkjet printing and impedance-based biosensing technology operating through a smartphone for clinical diagnostics. Biosens. Bioelectron. 196, 113737.

Rossetti, M., Merlo, R., Bagheri, N., Moscone, D., Valenti, A., Saha, A., Arantes, P.R., Ippodrino, R., Ricci, F., Treglia, I., Delibato, E., Van Der Oost, J., Palermo, G., Perugino, G., Porchetta, A., 2022. Enhancement of CRISPR/Cas12a trans-cleavage activity using hairpin DNA reporters. Nucleic Acids Res. 50 (14), 8377–8391. https://doi.org/10.1093/NAR/GKAC578.

Rossetti, M., Srisomwata, C., Urban, M., Rosati, G., Maroli, G., Yaman Akbay, G.H., Chailapakulb, O., Merkoçi, A., 2024. Unleashing inkjet-printed nanostructured electrodes and battery-free potentiostat for the DNA-based multiplexed detection of SARS-CoV-2 genes. Biosens. Bioelectron. 250, 116079 https://doi.org/10.1016/j.bios.2024.116079.

Rychert, J., 2019. Benefits and limitations of MALDI-TOF mass spectrometry for the identification of microorganisms. J. Infectiol. 2 (4), 1–5. https://doi.org/10.29245/2689-9981/2019/4.1142.

Santamaría, J., Toranzos, G.A., 2003. Enteric pathogens and soil: a short review. Int. Microbiol. 6 (1), 5–9. https://doi.org/10.1007/S10123-003-0096-1/METRICS.

Sundriyal, P., Bhattacharya, S., 2017. Inkjet-printed electrodes on A4 paper substrates for low-cost, disposable, and flexible asymmetric supercapacitors. ACS Appl. Mater. Interfaces 9 (44), 38507–38521. https://doi.org/10.1021/ACSAMI.7B11262/ASSET/IMAGES/LARGE/AM-2017-112626_0011.JPEG.

Swarts, D.C., Jinek, M., 2019. Mechanistic insights into the cis-and trans-acting DNase activities of Cas12a. Mol. Cell 73 (3), 589–600.

Swetha, P.D.P., Sonia, J., Sapna, K., Prasad, K.S., 2021. Towards CRISPR powered electrochemical sensing for smart diagnostics. Curr. Opin. Electrochem. 30, 100829.

Tagliaferri, S., Nagaraju, G., Panagiotopoulos, A., Och, M., Cheng, G., Iacoviello, F., Mattevi, C., 2021. Aqueous inks of pristine graphene for 3D printed microsupercapacitors with high capacitance. ACS Nano 15 (9), 15342–15353. https://doi.org/10.1021/ACSNANO.1C06535/ASSET/IMAGES/LARGE/NN1C06535_0006.JPEG.

Tani, A., Thomson, A.J., Butt, J.N., 2001. Methylene blue as an electrochemical discriminator of single- and double-stranded oligonucleotides immobilised on gold substrates. Analyst 126 (10), 1756–1759. https://doi.org/10.1039/B104260M.

Tauxe, R.V., 2002. Emerging foodborne pathogens. Int. J. Food Microbiol. 78 (1–2), 31–41. https://doi.org/10.1016/S0168-1605(02)00232-5.

Tyumentseva, M., Tyumentsev, A., Akimkin, V., 2023. CRISPR/Cas9 landscape: current state and future perspectives. Int. J. Mol. Sci. 24 (22), 16077 https://doi.org/10.3390/IJMS242216077/S1.

Ugboko, H.U., Nwinyi, O.C., Oranusi, S.U., Oyewale, J.O., 2020. Childhood diarrhoeal diseases in developing countries. https://doi.org/10.1016/j.heliyon.2020.e03690.

Urban, M., Rosati, G., Maroli, G., Pelle, F. Della, Bonini, A., Sajti, L., Fedel, M., Merkoçi, A., 2023. Nanostructure tuning of gold nanoparticles films via click sintering. Small, 2306167. https://doi.org/10.1002/SMLL.202306167.

Wang, W., Liu, J., Li, X., Lin, C., Wang, X., Liu, J., Ling, L., Wang, J., 2022. CRISPR/Cas12a-based biosensor for colorimetric detection of serum prostate-specific antigen by taking nonenzymatic and isothermal amplification. Sensor. Actuator. B Chem. 354, 131228.

WHO, 2008. Guidelines for Drinking-Water Quality: Second Addendum, vol. 1. World Health Organization Press, pp. 17–19. http://www.who.int/water_sanitation_health/dwq/secondaddendum20081119.pdf.

WHO, 2019. Safe water, better health. World Health Organization 1–67. https://apps.who.int/iris/bitstream/handle/10665/329905/9789241516891-eng.pdf.

Xiao, Y., Lai, R.Y., Plaxco, K.W., 2007. Preparation of electrode-immobilized, redox-modified oligonucleotides for electrochemical DNA and aptamer-based sensing. Nat. Protoc. 2 (11), 2875–2880. https://doi.org/10.1038/nprot.2007.413, 2007 2:11.

Xu, W., Jin, T., Dai, Y., Liu, C.C., 2020. Surpassing the detection limit and accuracy of the electrochemical DNA sensor through the application of CRISPR Cas systems. Biosens. Bioelectron. 155, 112100.

Yang, S., Rothman, R.E., 2004. PCR-based diagnostics for infectious diseases: uses, limitations, and future applications in acute-care settings. Lancet Infect. Dis. 4 (6), 337–348. https://doi.org/10.1016/S1473-3099(04)01044-8.

Yoo, S.M., Lee, S.Y., 2016. Optical biosensors for the detection of pathogenic microorganisms. Trends Biotechnol. 34 (1), 7–25.

Zamani, M., Yang, V., Maziashvili, L., Fan, G., Klapperich, C.M., Furst, A.L., 2022. Surface requirements for optimal biosensing with disposable gold electrodes. ACS Measurement Science Au 2 (2), 91–95. https://doi.org/10.1021/ACSMEASURESCIAU.1C00042/SUPPL_FILE/TG1C00042_SI_001.PDF.

Zavvar, T.S., Khoshbin, Z., Ramezani, M., Alibolandi, M., Abnous, K., Taghdisi, S.M., 2022. CRISPR/Cas-engineered technology: innovative approach for biosensor development. Biosens. Bioelectron. 214, 114501.

Zhang, D., Yan, Y., Que, H., Yang, T., Cheng, X., Ding, S., Zhang, X., Cheng, W., 2020. CRISPR/Cas12a-Mediated interfacial cleaving of hairpin DNA reporter for electrochemical nucleic acid sensing. ACS Sens. 5 (2), 557–562. https://doi.org/10.1021/ACSSENSORS.9B02461/ASSET/IMAGES/LARGE/SE9B02461_0002.JPEG.

Zhang, L., Jiang, H., Zhu, Z., Liu, J., Li, B., 2022. Integrating CRISPR/Cas within isothermal amplification for point-of-Care Assay of nucleic acid. Talanta 243, 123388.